HHS Public Access

Author manuscript

Small. Author manuscript; available in PMC 2017 February 01.

Published in final edited form as:

Small. 2016 February 03; 12(5): 612–622. doi:10.1002/smll.201501905.

Simultaneous or Sequential Orthogonal Gradient Formation in a 3D Cell Culture Microfluidic Platform

Sebastien G.M. Uzel[1], **Ovid C. Amadi**[2,3], **Taylor M. Pearl**[4], **Richard T. Lee**[3], **Peter T.C. So**[1,4], and **Roger D. Kamm**[1,4,*]

[1]Department of Mechanical Engineering, Massachusetts Institute of Technology (MIT), Cambridge, Massachusetts 02139

[2]Harvard-MIT Health Sciences and Technology, Cambridge, Massachusetts 02139

[3]Department of Stem Cell and Regenerative Biology, Harvard University, and Brigham and Women's Hospital, Cambridge, Massachusetts 02138

[4]Department of Biological Engineering, Massachusetts Institute of Technology (MIT), Cambridge, Massachusetts 02139

Abstract

Biochemical gradients are ubiquitous in biology. At the tissue level, they dictate differentiation patterning or cell migration. Recapitulating *in vitro* the complexity of such concentration profiles with great spatial and dynamic control is crucial in order to understand the underlying mechanisms of biological phenomena. Here we describe a microfluidic design capable of generating diffusion-driven, simultaneous or sequential, orthogonal linear concentration gradients in a three-dimensional cell-embedded scaffold. Formation and stability of the orthogonal gradients are demonstrated by computational and fluorescent dextran-based characterizations. We then explore system utility in two biological systems. First, we subject stem cells to orthogonal gradients of morphogens in order to mimic the localized differentiation of motor neurons in the neural tube. Similarly to *in vivo*, motor neurons preferentially differentiated in regions of high concentration of retinoic acid and smoothened agonist (acting as sonic hedgehog), in a concentration-dependent fashion. We then apply a rotating gradient to HT1080 cancer cells and investigate the change in migration direction as the cells adapt to a new chemical environment. We report that the response time is ~4h. These two examples demonstrate the versatility of this new design that could also prove useful in many applications including tissue engineering and drug screening.

Keywords

microfluidics; orthogonal gradients; dynamic chemotaxis; stem cell differentiation; cancer cell migration

[*]**Corresponding author:** Roger D. Kamm, Department of Biological Engineering, Department of Mechanical Engineering, Massachusetts Institute of Technology, 77 Massachusetts Avenue, Room NE47-318, Phone: (617) 253-6236, rdkamm@mit.edu.

1. Introduction

The complexity of biological tissue shapes and functions arises from the intricate superposition of stimuli presented to them in a space- and time-dependent fashion. These stimuli dynamically evolve as their sources and recipients move with respect to one another and regulate their response. Such cues include mechanical stretching or compression, electrical excitation or cell-cell signaling by paracrine or autocrine mechanisms. Important signaling cues are often provided as concentration gradients, which are ubiquitous in biology. Fundamental at the subcellular level to ensure homeostasis or ion transport,[1] they are also involved in long range cell signaling. Our ability to understand and manipulate these gradients is predicated on our ability to precisely emulate their evolution and regulation in controlled biophysical environments. Indeed, chemotaxis (the directed movement of cells in response to a chemical gradient) and morphogenesis (the concentration-dependent specification of cellular differentiation) are two phenomena driven largely by chemical gradients.[2,3]

Over the past several decades, multiple approaches have been developed to subject eukaryotic as well as prokaryotic cells to concentration gradients. Following the popular Boyden chamber that uses a porous insert to form a gradient by means of media compartmentalization,[4] numerous techniques improved on the concept, including the Zigmond or Dunn chambers, allowing live cell imaging.[5,6]

The application of soft lithography to the formation of microfluidic devices has vastly improved our ability to control concentration gradients,[7,8] along with a variety of other stimuli.[9–11] Flow-based devices are able to shape the gradient profiles over extended periods of time,[12–14] although the cultured cells are subjected to the added influence of shear stress. Relying on pure chemokine diffusion, other designs, often consisting of rows of microgrooves that isolate the medium channels from the cell chambers, alleviate the issue of shear stress while conserving the presence of steep gradients.[15–17] This approach was used to generate multidirectional gradients in solution for adherent, two-dimensional (2D) cultures.[18] A few groups proposed microfluidic devices capable of forming reversing,[19–21] oscillatory[22] or rotating gradients[23–25] in solution, although they were exclusively used in the context of chemotaxis in suspended or on adherent cultures (reviewed in [26,27]). The recent development of microfluidic devices capable of applying concentration gradients to three-dimensional (3D) hydrogel-based cell culture systems [15,28–32] not only increased the physiological relevance of such platforms, but it also made it possible to recapitulate tissue functions previously unattainable, such as the formation of a microvasculature [33,34] or the guidance of axons by chemotactic factors. [35]

Here, we describe a platform design that combines a 3D culture chamber with the ability to generate orthogonal linear gradients within the gel region. Two versions of the design are proposed, one aimed at forming simultaneous orthogonal gradients of two different molecules, the other capable of rotating by 90° an already established linear concentration profile. After characterizing the formation, stability and dynamics of the orthogonal gradients, we demonstrate their ability to induce a cellular response in contexts particularly relevant to multidirectional chemical gradients. The first application recapitulates the

localized differentiation of motor neurons in the developing neural tube by exposing mouse embryonic stem (ES) cells embedded in a collagen matrix to a combinatorial set of morphogen concentrations. The second application makes use of the 90° rotation of a linear gradient of chemokines to probe, for the first time, the time scale associated with 3D chemotactic adaptation of a population of cancer cells.

2. Results and discussion

2.1. Simultaneous or sequential orthogonal linear gradients can be stably generated in a 3D hydrogel

Static device—The cross-shaped design of this microfluidic platform (Figure 1) allows for the formation of a diffusion-driven linear gradient within its central gel region and its symmetry by a 90° rotation results in the ability to simultaneously (Figure 1a–c) or sequentially (Figure 1b, Figure S1) generate a second orthogonal gradient. This principle was experimentally validated by flowing in the medium channels two fluorescently-labelled dextrans, with diffusion coefficients representative of the morphogens and growth factors used in this study, and by monitoring the fluorescent signal as a way to assess their concentration.[36] The 70 kDa FITC-dextran, flowing in the top channels, established a vertical gradient (Figure 2ai) while the 3 kDa Texas Red-dextran, introduced via the right channels, developed into a horizontal gradient (Figure 2aii), orthogonal to the first one (Figure 2aiii). The time course of the concentration is plotted in Figure 2c, and was used to determine the diffusion coefficients of both dextrans, values that were consistent with past characterization of dextran diffusion in aqueous solutions.[37,38] Both dextran diffusion experimental assays behaved very similarly to what theory predicts, as assessed by computational simulations conducted on a simplified geometry (Figure 2b). The steadiness of the Texas Red-dextran at a level close to 50% beyond 5h over a period of 10h demonstrates the stability of the concentration profile. The concentration profiles in the central region (Figure 2d) were found to be highly linear with R^2 values of 0.9997 for the simulated result, and 0.9977 and 0.9925 for the FITC-dextran and the Texas Red-dextran, respectively. This linearity was the result of a pure diffusive process, guaranteed by a pressure balance across all reservoirs made possible by the y-junctions.

Computational simulations also allowed for characterization of the influence of the diffusion coefficient and flow rate on the concentration profiles. The range of diffusion coefficients was chosen to reflect the diffusivity of species used in the present study, and the flow rates were varied within values that were considered reasonable given the duration of the studies and the hardware constraints imposed by the experimental set-ups. Although the geometry of the system is symmetrical by a 90° rotation, the finite diffusive boundary layer gives rises to two slightly different solutions for the horizontal and vertical gradient configurations (Figure S6a). It was found that the concentration at the gel/medium interface at the furthest point along the channel (C_X), where the boundary layer is likely to be the thickest, increased slightly over the range of diffusion coefficients chosen, by no more than 4% of the maximum concentration (Figure S6b). C_X followed an opposite trend with respect to the flow rate with a value of 1 μL.min^{-1} providing a reasonable compromise between our desire

to maintain symmetric concentration distributions and to minimize the required volume of medium (Figure S6c).

Dynamic device—Computational and fluorescent dextran-based characterizations were also conducted on the dynamic version of the platform. Figure 3a and movie S1, S2 and S3 illustrate how switching the concentrations in 2 diagonally opposite channels by redirecting the flow via the membrane-valve system, rotates the gradient over time within the gel region by 90°. Quantitative comparison of the simulated and experimental time course of the concentrations at 5 locations of the central gel region exhibited excellent agreement (Figure 3b). The simulation reveals that, if averaged over the central region, the angle Θ_{grad} that a local gradient makes with the x-axis takes ~10, 20 and 40 min to reach 45° for a molecule of diffusivity 20, 10 and 5×10^{-7} $cm^2.s^{-1}$, respectively (Figure 3c).

We note that reducing the width of the gel region from 1.5 to 1 mm reduced the time to reach the initial steady state by a factor of 0.53. Moreover, regardless of the gel region width, the time to reach the second steady state after gradient rotation is reduced by a factor of 0.52 compared to the first steady state, resulting in a faster gradient turning than initial establishment (Figure 3b). This factor can be predicted by a scaling analysis: because the center point of the gel region remains constant at 50% of the bulk at all times once the first steady state is reached, the characteristic length of the diffusion process changes from the width of the region W to half its diagonal $\frac{1}{\sqrt{2}}W$. Since the diffusion time scales as the square of the distance, this leads to a theoretical gradient rotation time scale that is approximately half of that to first establish it.

2.2. Orthogonal gradients of retinoic acid and smoothened agonist can emulate the localized differentiation of motor neurons in the developing neural tube

The developing neural tube, the primordial structure for the central nervous system, is a polarized hollow elliptical cylinder that runs along a caudal-cranial axis in the vertebrate embryo. Retinoic acid (RA), produced in the somites, diffuses laterally into the neural tube to form a rostro-caudal gradient that is responsible for caudalizing the neuroepithelium and giving rise to spinal progenitors.[39,40] The notochord, a cylindrical structure lining the neural tube ventrally, and the floor plate, the most ventral part of the neural tube secrete the morphogen sonic hedgehog (SHH), forming a gradient that specifies progenitor identities in a concentration dependent manner[41] (Figure 4a). The combinatorial effect of those two orthogonally distributed morphogens contributes to the specification of the fate of the ventral spinal cord neurons,[42] and specifically motor neurons which arise in the presence of both RA and a high concentration of SHH, as evidenced both *in vivo* and *in vitro*.[40,43–45] Here we demonstrate that the proposed platform can serve as an *in vitro* model of such a phenomenon (Figure 4a), by subjecting ES-derived embryoid bodies (EB) embedded in a collagen matrix to two orthogonal gradients of retinoic acid and smoothened agonist (SAG), a small molecule activator of the SHH pathway[46,47] and commonly used for motor neuron differentiation.[48,49] SAG was preferred to SHH in this study for its higher diffusivity. The differentiation efficiency was assessed by measuring the level of GFP, expressed, in the HBG3 ES cell line, under the control of the promoter for Hb9, a motor neuron specific

transcription factor [40]. First, to validate the ability of the cells to differentiate within a collagen matrix and for the morphogens to induce a graded response similar to what was found with RA and SHH in past studies,[44,45] the assay was run in a 5 × 5 array of a 96 well plate. EBs had formed within the gel by day 2, and, on day 6, after exposure to RA and SAG, expression of GFP, indicative of the activation of Hb9, could be observed (Figure S7a). The heat map representing the combinatorial effect of RA and SAG not only confirms that the absence of either one of the morphogen leads to no motor neuron differentiation (consistent with past studies[45,48,50]), it also shows that the differentiation efficiency gradually increases with the concentration of both morphogens (Figure S7b and c). More importantly, it does so over a linearly increasing range of morphogen concentration, showing considerable promise for the microfluidic counterpart experiment below.

Now confident that the two morphogens are capable of differentiating ES cells into motor neurons within a 3D collagen gel and inducing a graded response, we conducted the experiment in the microfluidic static device described here (procedure detailed in the Methods section). Qualitatively, we notice that the macroscopic GFP signal, expressed, in Figure 4b, as the local fluorescent signal relative to the negative (absence of morphogens) and positive (uniform concentration of morphogens) controls, and representative of its local expression and indicative of the differentiation efficiency, is lower in the two branches of low exposure to the morphogens (Figure 4b, Figure S8ai) compared to the top-right part of the device, where levels of expression reach that of the positive control (Figure 4b, Figure S8ai, Figure S9). Note that data were collected in all four branches along with the central gel region to expand the ranges of concentration included in the quantitative analysis (Figure S8 and Methods section). This graded response is even more apparent in the matrix mapping (procedure described in the Methods section and Figure S8), where differentiation efficiency reaches maximum values in the top-right region of higher RA and SAG concentration (Figure 4c). This result is consistent with graded differentiation of adherent neural progenitors and 3D ES cells in 1D gradients of SHH generated in microfluidic devices.[14,29,51] The negative and positive controls ensured that the presence of the graded response was not an artifact of the platform but indeed due to the presence of the orthogonal gradients (Figure S9). The uniform GFP expression in the positive control also confirmed the absence of increased cell death in the central regions due to hypoxia or impaired nutrient transport. We also verified, by monitoring the displacement of individual GFP-positive cells via a time lapse recording of the entire differentiation process, that, although cells were found to be motile within their own neurospheres, did not migrate past the boundaries of the neurospheres. Therefore, these movements could not account for the overall graded response, and confirm that the graded differentiation efficiency was a consequence of the morphogen gradients. Contrary to well plate assays where the concentration discretization of the analysis is limited by the number of wells, applying a continuous range of concentration enables the users to decide *a posteriori* the binning size of the data analysis. Figure 4d shows four examples for a subdivision of the 0–100% concentration range into 2, 5, 7 and 10 intervals. For a coarse interpretation of the result, the 4 quadrant representation illustrates how the motor neuron differentiation pathway, quantitatively assessed here by GFP expression, effectively acts, in Boolean logic terminology, as an AND gate for the couple RA/SAG (Figure 4d and e) and confirms previous studies on mouse and human ES

cells.[40,45] A smaller binning size displays the concentration dependence of the differentiation process at a finer scale, here plotted along the first diagonal of the matrix (Figure 4d and f). It should be noted, however, that the bin size cannot be decreased beyond a point where the dimensions of the corresponding averaging area becomes smaller than the characteristic length of the investigated objects. In this instance, the average EB diameter of 160 μm determines a lower bound for the bin size, so the 1.5 mm wide gel region should be divided into no more than ~10 domains.

Another advantage of this platform is that it allows for cell-cell signaling between arising lineages, which, in contrast to well plate assays, better mimics the *in vivo* counterpart of an emulated tissue. It is likely that such paracrine interactions would contribute to differences observed between our motor neuron differentiation experiments within the microfluidic platform and the well plate assay. Moreover, while well plate and dish assays for adherent cultures remain the most convenient *in vitro* platforms, the more physiologically relevant 3D hydrogel cultures in such traditional platforms lack geometrical controllability. For those 3D cultures, microfluidic systems represent an attractive alternative, and, with automation of medium supply and data acquisition, could compete with the throughput of traditional assays.

Although a linear concentration profile has the advantage of exposing cell populations to a uniform gradient, many concentration-dependent biological phenomena occur over several orders of magnitude of the concentration of the molecule of interest, due to the inherent kinetics of the ligand-receptor complex and signaling cascade. This represents a potential limitation of our platform relative to well-plate assays since the latter would be more amenable to log-scale variations in concentration. Another limitation is the inherent sample-to-sample variability of the results compared to the smaller variation in the averages obtained with a well plate assay, explained by the larger dimension of the averaging regions. One way to compensate for this would be to use multiplexed microdevices.

2.3. Sequential orthogonal gradients can probe chemotactic response time

Cancer cell migration is a critical step in the metastatic cascade. It dictates how cells escape from the primary tumor and reach the blood or lymphatic circulation during intravasation, or how they migrate away from the vasculature at a distant site to form secondary metastases. A variety of cues are responsible for guiding this migration within the tumor microenvironment,[52] including chemical gradients via chemotaxis. We therefore tested the ability of our platform to expose a highly metastatic fibrosarcoma cell line HT1080[53] to a dynamic gradient and investigate the time scale associated with the response to a new chemical environment.

Four conditions were compared: *(i)* uniform serum-free medium, *(ii)* uniform 20% fetal bovine serum (FBS) medium, *(iii)* a static linear gradient (from 0 to 20% FBS, pointing to the right) and *(iv)* a rotating gradient (from 0 to 20% FBS, 8 h directed to the right followed by 7 h pointing up) (Figure 5a). Each trajectory shown represents the center of mass for the entire cell population tracked within the central gel region (Figure S10a). Tracked through images acquired by epifluorescence microscopy, these trajectories are equivalent to a projection on the x-y plane, although minimal migration is occurring in the z-direction. In

the absence of gradients, cells migrated randomly, while cells subject to the gradient migrated towards the high concentration (Figure 5a, c and d, Figure S10b and c), validating the ability of the platform to recapitulate 3D chemotaxis.[12,54]

Upon gradient rotation, we observed that the cells first continued migrating from left to right, then transitioned to a bottom-to-top trajectory following a change in the gradient direction after a short lag period (Figure 5a). This rotation of the direction of migration was quantitatively illustrated by comparing cell distribution Δ_y (Figure 5d) and the average displacements δ (Figure S10b and c) along y-axis between the static and dynamic cases. The forward migration index in the y-direction, as measure of the efficiency of forward migration transitioned from 4.4×10^{-3} to 90.6×10^{-3}.

We monitored cell speed V to ensure that the cells had reached their steady state migratory behavior before rotating the gradient. We found that all conditions began with migration speeds between 13 and 17 $\mu m.h^{-1}$. While cells subject to serum-free medium remained at a speed of 13 $\mu m.h^{-1}$, those exposed to 20% FBS medium, to the static gradient, or to the rotating gradient gradually increased their speed to values between 23 and 25 μm/h within ~4 h as FBS diffused into the gel region (Figure 5b). This chemokinesis phenomenon and the measured migration speeds were consistent with studies conducted with different cancer cell lines.[54,55]

Besides simply demonstrating a qualitative change in the migratory orientation, the ability to track single cell trajectories over time allows for quantification of the population migratory dynamic adaptation. The angle Θ_{mig} made by the migration direction of the center of mass with the x-axis (Figure 5e) for both the static gradient case remained centered around 0°, consistent with the trajectories of Figure 5a*iii*, while in the dynamic case, it started rising soon after the gradient began to rotate and eventually reached values close to 90°. If reaching the 45° line is used to characterize the time scale of direction change, the response of the cell population migration is observed ~250 min (4.15 h) after switching the concentration gradient. These data are to be compared with the time needed for the gradient itself to rotate. As mentioned above, species with diffusion coefficients in the ranges of 5 to 20×10^{-7} $cm^2.s^{-1}$ would take between 10 and 40 min to rotate (i.e. to reach on average 45°). Although the FBS constituents responsible for chemotaxis are not entirely known (growth factors like EGF being putative candidates), their diffusion coefficients likely fall within the range of the ones simulated here (for instance, $D_{EGF} = 12–15\times10^{-7}$ $cm^2.s^{-1}$[56]). It is therefore safe to assume that time needed for the cell population to sense the gradient rotation and significantly adapt their migration direction is between ~210 min (3.5 h) and ~240 min (4 h). This time lag translates into a residual migration along the x-axis after the gradient had rotated to become parallel to the y-axis (Figure S10d). Our mode of perturbation of the local chemical environment by gradient rotation minimally alters the other characteristics of the concentration profile; the average concentration in the central gel region remains constant during the switching process (Figure S6d) and the average amplitude Γ of the local gradients does not decrease by more than 25% of its steady state value (Figure S6e).

Since this platform is, to our knowledge, the first of its kind to allow the investigation of chemotactic dynamics in 3D, existing comparable data are scarce. In adherent cultures,

HL60 and neutrophils subject to alternating gradients of CXCL8 and IL-8, respectively, were found to reverse migration direction within a few minutes upon gradient inversion.[20,21] On the other hand, when exposed to interstitial flow, MDA-MB-231 cancer cells embedded in a collagen matrix took 36 h to align with the direction of flow.[57] These time scales differ by approximately one order of magnitude either way from the few hours we observed for the HT1080 cells in 3D, suggesting that different mechanisms pertain.

3. Conclusion

We successfully demonstrated the ability of the proposed device to generate simultaneous or time-dependent linear gradients within a 3D cell culture chamber. This new method of shaping the chemical microenvironment allowed us to emulate the localized appearance of motor neurons in the developing neural tube under the effect of morphogen gradients. Similar concentration profiles could be of use to investigate the combinatorial effects of molecules of interest, to mimic *in vivo* organogenesis and give rise to more complex and physiologically relevant tissue models. It is also unique in its ability to expose cells to ranges of concentrations of two molecules varying independently of each other, a feature that would not be possible in parallel or anti-parallel 1D gradient platforms and is therefore useful in probing the synergistic action of drugs or growth factors.

The dynamic version of the device was applied to the study of the chemotactic adaptation of cancer cells, which was found to occur at a time scale on the order of 4 h. Single cell analysis would allow for the monitoring of receptor repolarization, protrusion dynamics or morphological adaptation. Other migratory phenomena could benefit from this technology, including immune cell response and the dynamics of growth cone steering by chemoattractants.[58]

4. Materials and Methods

4.1. Device design

The static version of the proposed device consists of a cross-shaped, 1.5-mm-wide and 300-μm-thick, central gel region, lined by trapezoidal posts, and flanked by 1-mm wide medium channels (Figure 1a). The role of the posts is to retain by surface tension the hydrogel as it is being injected in its liquid form into the central region. The medium channels serve to provide nutrients, remove metabolic waste, and apply specific concentration boundary conditions. The device has 4 medium inlets, 4 gel filling ports, and 1 outlet. A first linear gradient arises in the central region from the diffusion into the gel of a chemokine flowing within 2 adjacent medium channels (Figure 1ci). A second linear gradient, orthogonal to the first one, can be generated by perfusing the next 2 adjacent channels with another molecule of interest (Figure 1cii). As a result of the device geometry, the concentration profile is invariant in the z-direction.

For the dynamic version of the device, the design was modified to perform an on-chip flow redirection in order to dynamically adapt the orientation of the gradient. A set of 4 open-at-rest pressure-actuated membrane valves were added to the design of a bottom microfluidic layer and were actuated via a top control layer (Figure 1b). Alternating the actuation of

opposite pairs of valves, from V_1 and V_3 to V_2 and V_4 (Figure S1) directs the fluid coming into inlets I_2 and I_3 to supply either one of the diagonally opposite medium channel around the gel region, while leaving the medium coming from inlets I_1 and I_4 unaltered, allowing for 2 gradient configurations, orthogonal to one another (Figure S1). To ensure hydrostatic pressure balance across the gel region that could arise from heterogeneous medium channel lengths and to prevent fluid convection that would skew the linear nature of the gradient, the width along medium channels was modified to compensate length variation. This yielded a match, across all channels between resistivity values that scale as $\int \frac{ds}{w(s).h^3}$, where *ds* is an element of contour along the medium channel, *w(s)* is the channel width at the position *s*, and *h* is the constant height of the channel.[59]

4.2. Wafer and PDMS device fabrication and assembly

The fabrication of the wafers and devices was carried out similarly to procedures previously reported.[57,60,34] Briefly, molds were made by photo polymerizing a layer of SU-8 photoresist (MicroChem, MA) on a 4-inch silicon wafer. Upon completion of SU-8 development, the wafer was silanized to render the surface non-adhesive. All microfluidic chips were made out of a 10:1 mix of Polydimethyldiloxane (PDMS) (Sylgard 184, Ellsworth Adhesives, Germantown, WI) and curing agent.

Static version—The PDMS was poured onto the mold and, after ~30 min of degassing in a desiccator, was allowed to polymerize at 80°C for a minimum of 2 h. Subsequently, the PDMS was extracted from the mold and individual devices were cut from the PDMS with a 3.5 cm cylindrical punch. Medium, gel filling and outlet ports were created using 4, 1 and 2 mm biopsy punches, respectively. After wet and dry sterilization of the device, the surface was treated with plasma (Harrick Plasma, NY) for 45 s, then bonded to a glass slide. Immediately after plasma bonding, all channels were filled with PBS containing 1 mg/ml of poly-D-lysine (PDL) to enhance adhesion of the collagen matrix to the walls of the gel region. Devices were incubated overnight, then washed three times with DI water and allowed to dry and recover hydrophobicity for 1 day.

Dynamic version—Prior to silanization of the wafer of the microfluidic layer, the bottom part of the microfluidic channels facing the valve control area was made trapezoidal to improve the sealing by gently scraping out a wedge of SU-8 near the wafer with a gauge 26 needle at a 35° angle (Figure S2). This was facilitated by the rather thick channel layer. This simple method alleviated the need for cumbersome fabrication techniques to obtain rounded channels[61] and allowed for localized wafer modification contrary to full wafer reflow techniques.[62]

The control layer was fabricated in the same way as the static device. Access ports were punched with a diameter of 2 mm. To form the thin membranes serving as valves, the microfluidic bottom layer was generated by positioning a silanized transparency sheet on top of some uncured PDMS poured over the wafer, while avoiding trapping bubbles, and applying pressure with a flat weight; a method similar to a previously published one.[63] The presence of 4 supports, ~ 100 μm taller than the microfluidic channels, ensured a consistent membrane thickness throughout the wafer (Figure S3a, right). Upon curing, the plastic sheet

was gently peeled off, resulting in a flatter profile than obtained by spin coating the wafer, which tends to cause variations in the surface height (Figure S3a, left). The bottom surface of the control devices and the top surface of the microfluidic layer (still on the wafer) were plasma treated for 45 s and assembled under a stereomicroscope to ensure proper alignment. The PDMS was gently cut with a scalpel at the dimensions of the control device and the two-layer device was peeled off of the wafer. A 1-mm biopsy punch was used to form the gel filling ports and remove the membrane blocking the bridge area allowing the fluidic channels to cross each other (Figure S3b). The outlet and inlet ports were formed with 2-mm and 2.5-mm biopsy punches, respectively. The formation of the inlet ports was guided by a template to ensure proper fitting with the medium reservoir (Figure S4b). The devices were then plasma treated and assembled onto a glass slide before being sterilized for cell culture.

4.3. Gel filling and cell seeding

For both versions of the device, rat tail type I collagen (Corning) was used as the culture scaffold. 10x PBS containing phenol red, NaOH (0.5 N), DI water and collagen were mixed on ice, in that order, in ratios that would dilute the concentrated collagen stock solution (ranging from 3 to 4 mg/ml) to a 2 mg/ml, isotonic solution of pH 7.4.

For characterization experiments, plain gel solution was injected to the devices through the gel filling ports with a 20 μl pipette tip. To prevent pressure increase that would result in the gel solution bulging out of the gel region, the solution was injected through each of the 4 branches of the gel region, one at a time. The device was then placed in a humidity box to prevent evaporation and the gel allowed to polymerize in the incubator for 20 min, after which medium or PBS was backfilled from the outlet into the medium channels. The devices were left in the humidity chamber until used.

For the experiments involving cells, the same 2 mg/ml mixture was used to resuspend a pellet of cells in order to reach an appropriate cell density for each experiment. To prevent cells from settling on the floor of the device during polymerization, the devices were rotated upside down for 4 min, before being rotated upright for the remaining 16 min.

In the dynamic version of the device, prior to gel seeding, the valves were pre-filled by compressing PBS into the control channels for ~20 min. The gas permeability of PDMS allowed for the liquid to chase air and to fill up the dead-end channel, preventing bubble from forming upon actuation of the valves.

4.4. Cell culture

Mouse ES cells HBG3 (HB9-GFP), a kind gift from Pr. Hynek Wichterle, Columbia University, NY, were cultured on a confluent monolayer of mouse embryonic fibroblasts (Applied StemCell, CF-1 MEF Feeder Cells, P3, irradiated, ASF-1217), plated on gelatin coated dishes, in culture medium consisting of Embryomax ES Dulbecco's Modified Eagle's Medium (DMEM) (Millipore Chemicon), 15% ES-qualified fetal bovine serum (FBS) (Invitrogen), 1% nucleosides (Millipore Chemicon), 1% non-essential amino acids (Millipore Chemicon), 1% penicillin-streptomycin (Invitrogen), 1% L-glutamine (Invitrogen), 0.1 mM β-mercaptoethanol (Sigma), 0.1% leukemia inhibitory factor (EMD Millipore, LIF2010).[48] HT1080-mCherry-H2B fibrosarcoma cells[28] were cultured in

DMEM (Invitrogen) supplemented with 10% FBS, 1% L-glutamine and 1% penicillin-streptomycin.

4.5. Orthogonal gradient and differentiation assay: set-up and data acquisition

ES cells were trypsinized and preplated for 30 min onto 0.1% gelatin coated dishes to eliminate fibroblasts and differentiated cells. The non-adherent cells were collected, counted, spun down and resuspended in the collagen gel at a density of 1×10^6 cells/ml before being seeded into the PDL-coated devices (see “gel filling” section above). Upon gel polymerization, differentiation medium was supplied to the medium channels. The differentiation medium consisted of 1:1 Advanced DMEM/F-12 (Invitrogen) / Neurobasal (Invitrogen), 10% knockout serum replacement (Invitrogen), 1% penicillin-streptomycin, 1% L-glutamine, β-mercaptoethanol (0.1 mM).[48] On day 2, tubing and reservoirs were mounted onto the devices (see “tubing and reservoir assembly” section). The devices were placed back into the incubator and the reservoirs were slightly backfilled with plain medium at a flow rate of 100 $\mu L.min^{-1}$ via a syringe pump (Harvard Apparatus, Cambridge, MA). In order to prevent extensive medium circulation and mixing during reservoir fill up, the medium was supplied with a custom-made square-shaped pipet tip adapter mounted to a linear multichannel pipettor (Figure S4a*iii*). The orthogonal gradient was formed by supplementing the media with retinoic acid (RA) (Sigma), and smoothened agonist (SAG) (EMD). From bottom left and in a clockwise order, the morphogens were supplemented as such: nothing, RA, RA+SAG and SAG. Both were supplied at a concentration of 1 μM, as suggested in the literature as the optimum dosage for motor neuron differentiation.[48] A total of 3 ml was supplied to each reservoir. An initial 0.5 ml/reservoir was purged at 100 $\mu L.min^{-1}$, after which flow rate was set to 4 $\mu L.min^{-1}$. Medium was replenished with 2 ml after 36 hours. On day 5, medium was replaced by plain differentiation medium supplemented with 10 ng/ml of both glia-derived neurotrophic factor (GDNF) (R&D systems) and ciliary neurotrophic factor (CNTF) (R&D systems). After each medium change, flow rate was increased temporarily to reset the boundary conditions. By day 6, devices were fixed with 4% paraformaldehyde and imaged by confocal microscopy (Olympus FV-1000). To minimize the scanning time and because images will subsequently be projected along the z axis, the pinhole was wide open at 800 μm diameter increasing the depth of field. Eight slices were acquired per tile for a total of 32 tiles to cover the entire gel surface area.

4.6. Rotating gradient and migration assay: set-up and data acquisition

Migration experiments were conducted after the HT1080 cells, seeded at a density of 0.5×10^6 cells/ml, recovered overnight in starving medium consisting in 0.5% FBS in order to reduce migration and matrix degradation. The chemotactic gradients were generated by supplying 2 adjacent channels with FBS-free medium, while the medium in the opposite 2 channels contained 20% FBS along with 70 kDa dextran-FITC to monitor the formation and stability of the gradient throughout the experiment. After bubble removal (see “bubble removal” section) and tubing and reservoir assembly (see “tubing and reservoir assembly” section) the devices were placed on the stage of a Axiovert 200 inverted microscope (Zeiss, Germany) contained in a humidified and CO2- and temperature-controlled environmental chamber. Outlet tubing was connected to a syringe pump and the valves were pressurized by

placing a mass on a vertically oriented 10 ml syringe resulting in a power-free steady pressure of 12 Psi. An initial flow rate of 100 μL.min^{-1} was applied for 2 min to purge the channels and establish proper boundary conditions, then reduced to 4 μL.min^{-1}. Phase contrast, mCherry and GFP images collected at the mid-plane with a 10x objective were acquired every 15 min for 16 h with the Axiovision software (Zeiss). For the experiments with gradient rotation, the valves were switched at t = 8 h and the flow rate was increased to 100 μL.min^{-1} for 2 min to purge the channels from the previous media.

4.7. Bubble removal

Complete bubble removal from the medium, gel filling ports and control channels was crucial to prevent bubble growth that would, in turn, lead to gel destruction or flow obstruction. We employed a technique inspired by [64]. However, instead of applying compressed fluid directly into the channel that would cause delamination of the PDMS layers, the entire device, immersed in pre-warmed PBS, was pressurized in a custom-made polycarbonate chamber at ~16 psi for 20 min (Figure S5a). This procedure completely removed all bubbles with no adverse effect on cell survival or behavior (Figure S5b). Failure to immerse the device in PBS would result in reappearance of the bubbles within 5 min following pressure release (Figure S5c and d).

4.8. Statistical analysis

Statistical analysis was done in Prism (Graphpad Software, Inc, San Diego, CA). Statistical significance analysis was conducted with ANOVA and all tests resulting in a p-value less than 0.05 were considered statistically significant.

Supplementary Material

Refer to Web version on PubMed Central for supplementary material.

Acknowledgements

The authors would like to thank Hynek Wichterle and Thomas Jessell for kindly sharing their cell line. We also thank Andrew McMahon and Yuichi Nishi for their precious insight on stem cell biology. Help from Mark Belanger at the Edgerton student shop was greatly appreciated. We thank the Lu lab for making their plate reader available. We are grateful to Ron Weiss, Martha Gillette and William Polacheck and to Michelle Chen and Ran Li for the insightful discussions and comments.

Funding from the National Science Foundation Science and Technology Center for Emergent Behaviors of Integrated Cellular Systems (CBET-0939511) and from NIH NRSA / UNCF Merck is greatly appreciated.

References

[1]. Dubyak GR. Adv. Physiol. Educ. 2004; 28:143. [PubMed: 15545343]
[2]. Gurdon JB, Bourillot PY. Nature. 2001; 413:797. [PubMed: 11677596]
[3]. Jin T, Xu X, Hereld D. Cytokine. 2008; 44:1. [PubMed: 18722135]
[4]. Boyden S. J. Exp. Med. 1962; 115:453. [PubMed: 13872176]
[5]. Zicha D, Dunn G. a, Brown a F. J. Cell Sci. 1991; 99(Pt 4):769. [PubMed: 1770004]
[6]. Zigmond SH. Jounal cell Biol. 1977; 75:606.
[7]. Xia Y, Whitesides GM. Annu. Rev. Mater. Sci. 1998; 28:153.

[8]. Jeon NL, Dertinger SKW, Chiu DT, Choi IS, Stroock AD, Whitesides GM. Langmuir. 2000; 16:8311.

[9]. Polacheck WJ, Li R, Uzel SGM, Kamm RD. Lab Chip. 2013; 13:2252. [PubMed: 23649165]

[10]. Li J, Lin F. Trends Cell Biol. 2011; 21:489. [PubMed: 21665472]

[11]. Pavesi A, Piraino F, Fiore GB, Farino KM, Moretti M, Rasponi M. Lab Chip. 2011; 11:1593. [PubMed: 21437315]

[12]. Wang S-J, Saadi W, Lin F, Minh-Canh Nguyen C, Li Jeon N. Exp. Cell Res. 2004; 300:180. [PubMed: 15383325]

[13]. Dertinger SKW, Jiang X, Li Z, Murthy VN, Whitesides GM. Proc. Natl. Acad. Sci. U. S. A. 2002; 99:12542. [PubMed: 12237407]

[14]. Park JY, Kim SK, Woo DH, Lee EJ, Kim JH, Lee SH. Stem Cells. 2009; 27:2646. [PubMed: 19711444]

[15]. Saadi W, Rhee SW, Lin F, Vahidi B, Chung BG, Jeon NL. Biomed. Microdevices. 2007; 9:627. [PubMed: 17530414]

[16]. Millet LJ, Stewart ME, Nuzzo RG, Gillette MU. Lab Chip. 2010; 10:1525. [PubMed: 20390196]

[17]. Keenan TM, Frevert CW, Wu A, Wong V, Folch A. Lab Chip. 2010; 10:116. [PubMed: 20024059]

[18]. Harink B, Le Gac S, Barata D, van Blitterswijk C, Habibovic P. Electrophoresis. 2015; 36:475. [PubMed: 25263102]

[19]. Meier B, Zielinski A, Weber C, Arcizet D, Youssef S, Franosch T, Rädler JO, Heinrich D. Proc. Natl. Acad. Sci. U. S. A. 2011; 108:11417. [PubMed: 21709255]

[20]. Liu Y, Sai J, Richmond A, Wikswo JP. Biomed. Microdevices. 2008; 10:499. [PubMed: 18205049]

[21]. Irimia D, Liu S-Y, Tharp WG, Samadani A, Toner M, Poznansky MC. Lab Chip. 2006; 6:191. [PubMed: 16450027]

[22]. Skoge M, Yue H, Erickstad M, Bae A, Levine H, Groisman A. Proc. Natl. Acad. Sci. 2014; 111:1.

[23]. Atencia J, Morrow J, Locascio LE. Lab Chip. 2009; 9:2707. [PubMed: 19704987]

[24]. Choi E, Chang H, Young Lim C, Kim T, Park J. Lab Chip. 2012; 12:3968. [PubMed: 22907568]

[25]. Brett M-E, Deflorio R, Stone DE, Eddington DT. Lab Chip. 2012; 12:3127. [PubMed: 22760670]

[26]. Wu J, Wu X, Lin F. Lab Chip. 2013; 13:2484. [PubMed: 23712326]

[27]. Irimia D. Annu. Rev. Biomed. Eng. 2010; 12:259. [PubMed: 20450351]

[28]. Zervantonakis IK, Hughes-Alford SK, Charest JL, Condeelis JS, Gertler FB, Kamm RD. Proc. Natl. Acad. Sci. U. S. A. 2012; 109:13515. [PubMed: 22869695]

[29]. Amadi OC, Steinhauser ML, Nishi Y, Chung S, Kamm RD, McMahon AP, Lee RT. Biomed. Microdevices. 2010; 12:1027. [PubMed: 20661647]

[30]. Haessler U, Kalinin Y, Swartz M. a, Wu M. Biomed. Microdevices. 2009; 11:827. [PubMed: 19343497]

[31]. Farahat, W. a., Wood, LB., Zervantonakis, IK., Schor, A., Ong, S., Neal, D., Kamm, RD., Asada, HH. PLoS One. 2012; 7 DOI 10.1371/journal.pone.0037333.

[32]. Mosadegh B, Huango C, Park JW, Shin HS, Chung BG, Hwang SK, Lee KH, Kim HJ, Brody J, Jeon NL. Langmuir. 2007; 23:10910. [PubMed: 17910490]

[33]. Shin Y, Han S, Jeon JS, Yamamoto K, Zervantonakis IK, Sudo R, Kamm RD, Chung S. Nat. Protoc. 2012; 7:1247. [PubMed: 22678430]

[34]. Vickerman V, Blundo J, Chung S, Kamm R. Lab Chip. 2008; 8:1468. [PubMed: 18818801]

[35]. Kothapalli CR, van Veen E, de Valence S, Chung S, Zervantonakis IK, Gertler FB, Kamm RD. Lab Chip. 2011; 11:497. [PubMed: 21107471]

[36]. Banerjee A, Shuai Y, Dixit R, Papautsky I, Klotzkin D. J. Lumin. 2010; 130:1095.

[37]. Arrio-Dupont M, Cribier S, Foucault G, Devaux PF, d'Albis a. Biophys. J. 1996; 70:2327. [PubMed: 9172756]

[38]. Lawrence JR, Wolfaardt GM, Korber DR. Appl Env. Microbiol. 1994; 60:1166. [PubMed: 16349228]

[39]. Maden M. Nat. Rev. Neurosci. 2007; 8:755. [PubMed: 17882253]
[40]. Wichterle H, Lieberam I, Porter J. a, Jessell TM. Cell. 2002; 110:385. [PubMed: 12176325]
[41]. Dessaud E, McMahon AP, Briscoe J. Development. 2008; 135:2489. [PubMed: 18621990]
[42]. Briscoe J, Ericson J. Curr. Opin. Neurobiol. 2001; 11:43. [PubMed: 11179871]
[43]. Okada Y, Shimazaki T, Sobue G, Okano H. Dev. Biol. 2004; 275:124. [PubMed: 15464577]
[44]. Ericson J, Briscoe J, Rashbass P, van Heyningen V, Jessell TM. Cold spring Harb. Symp. Quant. Biol. 1997; 62:451. [PubMed: 9598380]
[45]. Li X-J, Du Z-W, Zarnowska ED, Pankratz M, Hansen LO, Pearce RA, Zhang S-C. Nat. Biotechnol. 2005; 23:215. [PubMed: 15685164]
[46]. Chen JK, Taipale J, Young KE, Maiti T, Beachy P. a. Proc. Natl. Acad. Sci. U. S. A. 2002; 99:14071. [PubMed: 12391318]
[47]. Frank-Kamenetsky M, Zhang XM, Bottega S, Guicherit O, Wichterle H, Dudek H, Bumcrot D, Wang FY, Jones S, Shulok J, Rubin LL, Porter J. a. J. Biol. 2002; 1:10. [PubMed: 12437772]
[48]. Wichterle H, Peljto M. Curr. Protoc. Stem Cell Biol. 2008:1. [PubMed: 18770634]
[49]. Wu C-Y, Whye D, Mason RW, Wang W. J. Vis. Exp. 2012:1.
[50]. Wada T, Honda M, Minami I, Tooi N, Amagai Y, Nakatsuji N, Aiba K. PLoS One. 2009; 4 DOI 10.1371/journal.pone.0006722.
[51]. Fung W-T, Beyzavi A, Abgrall P, Nguyen N-T, Li H-Y. Lab Chip. 2009; 9:2591. [PubMed: 19680583]
[52]. Polacheck WJ, Zervantonakis IK, Kamm RD. Cell. Mol. Life Sci. 2013; 70:1335. [PubMed: 22926411]
[53]. Rasheed S, Nelson-Rees W. a, Toth EM, Arnstein P, Gardner MB. Cancer. 1974; 33:1027. [PubMed: 4132053]
[54]. Zengel P, Nguyen-Hoang A, Schildhammer C, Zantl R, Kahl V, Horn E. BMC Cell Biol. 2011; 12:21. [PubMed: 21592329]
[55]. Niggli V, Schmid M, Nievergelt A. Biochem. Biophys. Res. Commun. 2006; 343:602. [PubMed: 16554034]
[56]. Thorne RG, Hrabetová S, Nicholson C. J. Neurophysiol. 2004; 92:3471. [PubMed: 15269225]
[57]. Polacheck WJ, Charest JL, Kamm RD. Proc. Natl. Acad. Sci. U. S. A. 2011; 108:11115. [PubMed: 21690404]
[58]. Dickson BJ. Science. 2002; 298:1959. [PubMed: 12471249]
[59]. Han LS. J. Appl. Mech. 1960; 27:403.
[60]. Yamamoto K, Zervantonakis IK, Sudo R, Kamm RD. Nature. 2012
[61]. Dy AJ, Cosmanescu A, Sluka J, Glazier J. a, Stupack D, Amarie D. J. Micromechanics Microengineering. 2014; 24:057001.
[62]. Unger, M. a, Chou, HP., Thorsen, T., Scherer, a, Quake, SR. Science. 2000; 288:113. [PubMed: 10753110]
[63]. Liu C, Cui D, Cai H, Chen X, Geng Z. Electrophoresis. 2006; 27:2917. [PubMed: 16721901]
[64]. Kang JH, Kim YC, Park J-K. Lab Chip. 2008; 8:176. [PubMed: 18094777]
[65]. Dodon C, Peresypkin A, Rengarajan K, Wu S, Nickerson J. Curr Eye Res. 2002; 24:66. [PubMed: 12187497]
[66]. Schultz SG, Solomon AK. J. Gen. Physiol. 1961; 44:1189. [PubMed: 13748878]

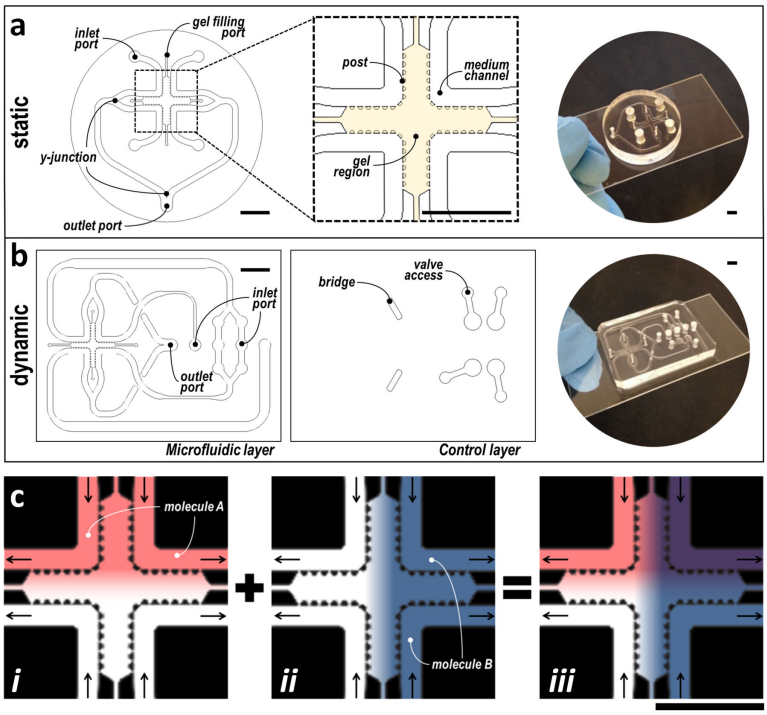

Figure 1. Microfluidic design and principle of orthogonal gradient generation

(a) The static version of this microfluidic device consists of a cross-shaped gel region lined by trapezoidal posts and flanked by medium channels. **(b)** The dynamic version consists of a two-layer device: a bottom microfluidic layer featuring the same cross-shaped gel region and a top control layer allowing for valve actuation as well as serving as a bridge. **(c)** Illustration of the formation of two concentration gradients orthogonal to each other. Arrows indicate the direction of flow. All scale bars: 5 mm.

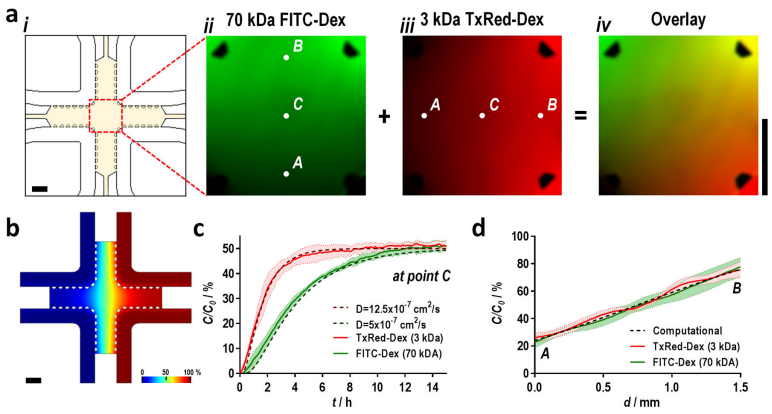

Figure 2. Experimental and computational gradient characterization in the static device

(a) Experimental demonstration of the formation of two orthogonal gradients obtained with 70 kDa FITC-dextran (green) and 3 kDa Texas Red-dextran (red). **(b)** Gradient formation simulated in the simplified computational model, illustrated by a heat map representing the fraction of the bulk concentration (C_0). **(c)** Time course of the concentration C at the center point of the gel region (point C in a*ii*-a*iii*), expressed as a fraction of the bulk concentration (C_0), for 70 kDa FITC-dextran (green) and 3 kDa Texas Red-dextran (red) compared to the simulated profiles for molecules of diffusion coefficient 5×10^{-7} (green dashed line) and 12.5×10^{-7} cm^2/s (red dashed line). **(d)** Steady state linear concentration profiles plotted between points A and B (a*ii*-a*iii*) as afunction of the distance *d* for both dextran molecules compared to the simulated profiles. Shaded bands in (c) and (d) represent standard deviation. All scale bars: 1 mm.

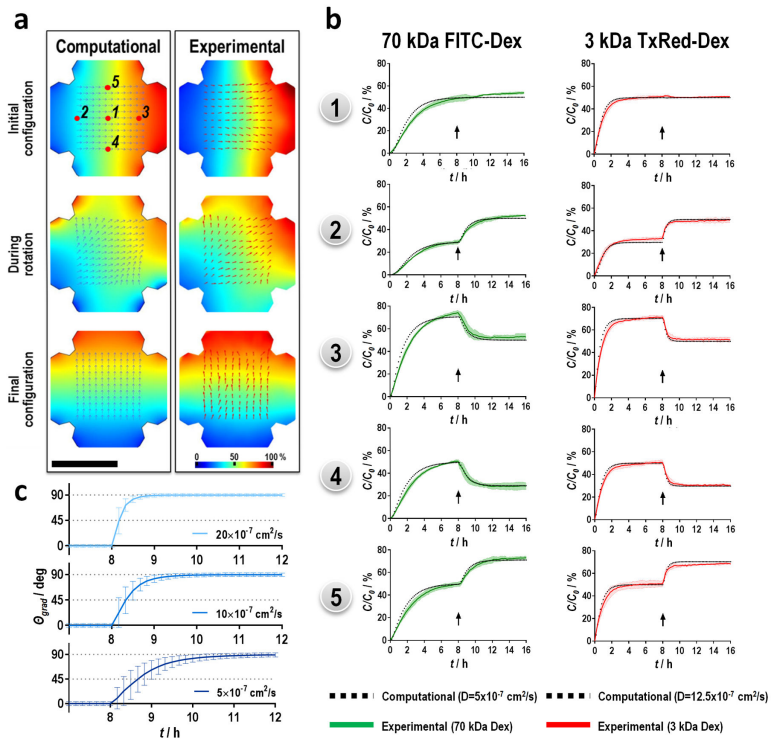

Figure 3. Experimental and computational gradient characterization in the dynamic device

(a) Experimental and simulated concentration profiles before, during and after gradient rotation. Each arrow represents the local concentration gradient direction and amplitude. **(b)** Time course of the concentration expressed as a fraction of the bulk (C/C_0) at 5 points within the gel region (as shown in (a)) for 70 kDa FITC-dextran (green) and 3 kDa Texas Red-dextran (red) compared to the simulated profiles for molecules of diffusion coefficient 5×10^{-7} (green dashed line) and 12.5×10^{-7} cm^2/s (red dashed line). Black arrows indicate gradient switch. **(c)** Time course of the average angle Θ_{grad} formed between the simulated gradient direction and the x-axis for 3 different diffusion coefficients. Shaded bands and error bars represent standard deviation.

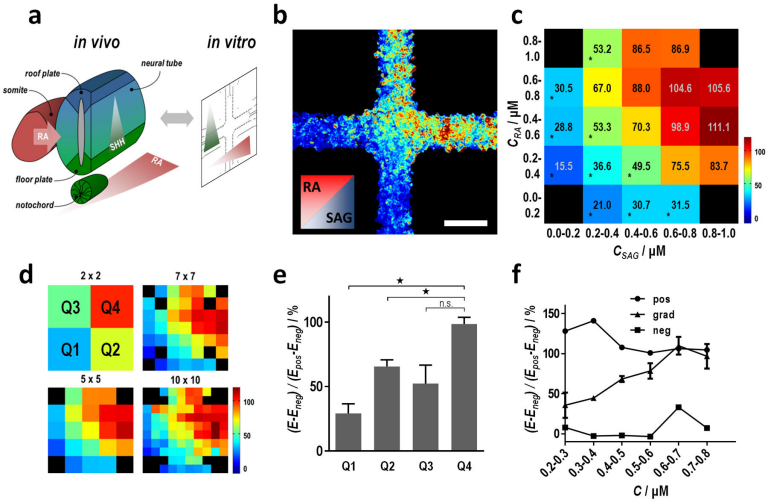

Figure 4. Demonstration of the effect of orthogonal gradients of retinoic acid (RA) and smoothened agonist (SAG) on the localized differentiation of motor neurons

(a) Schematic comparing the morphogen concentration profiles in the developing neural tube and their counterpart in the microfluidic device. **(b)** Heat map representing the local expression of GFP expression in the neurospheres normalized by the average GFP expression in the positive and negative controls control ($E-E_{neg}/E_{pos}-E_{neg}$). Average of two replicates, each comprised of 3 devices. Scale bar: 2 mm. **(c)** Matrix representation of the heat map in (b). Each value corresponds to the local average calculated over the range of concentrations showed on the x- and y-axes, as detailed in Figure S8 (black squares indicate excluded data, see Methods section). Stars indicate a statistically significant result with respect to the maximum data point ($p<0.05$). **(d)** Four matrix representations with varying binning size (black squares indicate excluded data). **(e)** Quadrant analysis of the result in (b) for a binning size of 50% ((d), 2×2). **(f)** Graph representing the relative GFP expression along the diagonal y=x as a function of the concentration C of RA and SAG for a binning size of 10% ((d), 10×10) (pos: positive control, grad: orthogonal gradients, neg: negative control). All error bars: SEM, ns: not significant.

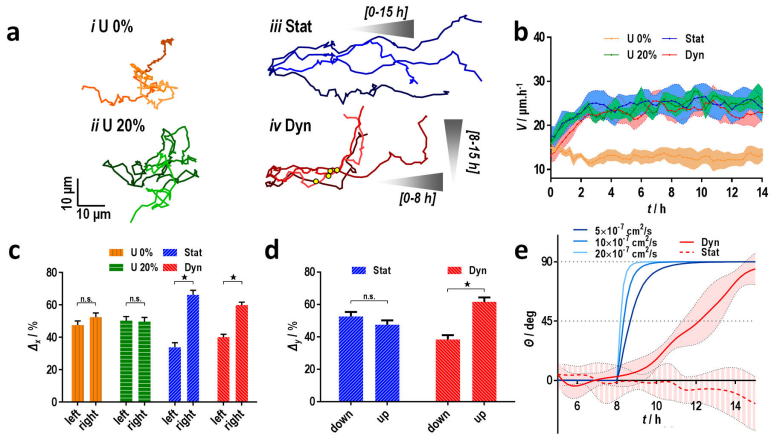

Figure 5. Demonstration of the effect of gradient rotation in the chemotaxis of HT1080 cells

(a) Trajectories of the centers of mass for the 4 tested conditions (each condition is the average of 4 replicates). The grey triangles indicate the direction of the gradient. The yellow dots indicate the beginning of gradient rotation. **(b)** Time course of the average migration speed V. **(c)** Final cell distribution Δ_x along the x-axis with respect to their initial position. **(d)** Final cell distribution Δ_y along the y-axis with respect to their position at t = 8 h **(e)** Time course of the average cell migration angle Θ_{mig} (red) and simulated gradient angle Θ_{grad} (blue) with respect to the x-axis. U: uniform, Stat: static gradient, Dyn: dynamic gradient. Shaded bands and error bars indicate standard errors, ns: not significant.